The relationship between linearised 3D and 2DH models for tidally dominated shallow waters

Rozendaal, Marco P.; Dijkstra, Yoeri M.; Schuttelaars, Henk M.

DOI
10.1016/j.ocemod.2024.102330

Publication date
2024

Document Version
Final published version

Published in
Ocean Modelling

Citation (APA)
Rozendaal, M. P., Dijkstra, Y. M., & Schuttelaars, H. M. (2024). The relationship between linearised 3D and 2DH models for tidally dominated shallow waters. *Ocean Modelling*, *188*, Article 102330. https://doi.org/10.1016/j.ocemod.2024.102330

Ocean Modelling 188 (2024) 102330

Contents lists available at ScienceDirect

Ocean Modelling

journal homepage: www.elsevier.com/locate/ocemod

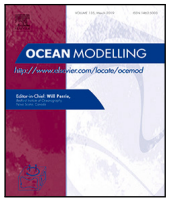

The relationship between linearised 3D and 2DH models for tidally dominated shallow waters

Marco P. Rozendaal *, Yoeri M. Dijkstra, Henk M. Schuttelaars

Delft Institute of Applied Mathematics, Delft University of Technology, Delft, The Netherlands

ARTICLE INFO

Keywords:
Idealised model
3D model
2DH model
3D friction formulation

ABSTRACT

The water motion computed using 3D and 2DH models in tidally dominated shallow waters can, in some cases, differ significantly. In 2DH models, bed friction is typically parametrised in terms of the depth-averaged velocity, whereas in 3D models, typically the near-bed velocity is used. This difference causes the bed shear stress in 2DH models to point towards the depth-averaged velocity, whereas in 3D models, it points towards the near-bed velocity, which are not necessarily the same. Focussing on linearised barotropic models, we derive an exact friction parametrisation for 2DH models such that the same depth-averaged dynamics are described as in the corresponding 3D model. The result is a convolutional friction formulation where the instantaneous friction depends on the present and past velocities, thus modifying the traditional 2DH friction formulation that only depends on the present depth-averaged velocity. In the case of harmonic (tidal) waves, this parametrisation has a clear physical interpretation and shows that the near-bed velocity should be parametrised as a rotated, deformed and phase shifted variant of the depth-averaged velocity. We demonstrate that in certain regions of the parameter space, it may be impossible to calibrate a 2DH model that uses a traditional friction law to reproduce the water levels from a 3D model, showing that the 3D friction formulation can be crucial to capture the 3D dynamics within a depth-averaged model. This phenomenon is explored in detail in a narrow well-mixed estuary.

1. Introduction

Estuaries and shelf seas are important coastal features that can be found all over the world. The water motion in these shallow regions is not only important to understand for safety reasons, but is also crucial for the transport of constituents, such as salt, sediments and nutrients (Wong, 1994; Li and O'Donnell, 1997; Stacey et al., 2001). The vertical structure of the water motion plays an essential role in mixing and redistributing these substances throughout the water column (Fischer, 1972; Dyer, 1974). As a consequence, the water motion is inherently three dimensional, even in these shallow regions. Since tides are an important driver of the water motion, their three-dimensional structure is important to be understood. However, much of our understanding is based on two-dimensional horizontal (2DH) models, with a specific focus on linearised 2DH barotropic models (Taylor, 1921; Friedrichs, 2010; Roos et al., 2011). These models have, for example, been used to explain quarter wavelength resonance (Defant, 1961), cross-channel half-wave resonance (Huthnance, 1980), radiation damping (Garrett, 1975) and amphidromic points (Taylor, 1921). In these approaches, it is implicitly assumed that a depth-averaged model is able to capture the three-dimensional water motion sufficiently well in order to describe, for example, the water levels, transport of water and derived properties, such as resonance lengths and characteristics.

The key difference between 3D and 2DH models is that a 3D model resolves the vertical structure of the velocity profile whereas a 2DH model only describes the behaviour of the depth-averaged velocity. By only resolving the depth-averaged velocity, it follows that processes that depend on a local velocity, e.g., at the free surface or bed, must be parametrised in terms of the depth-averaged velocity. The bed shear stress $\boldsymbol{\tau}_b$ is often a dominant dissipation mechanism in shallow waters, so an accurate description of this stress is crucial. In 3D models, the bed shear stress is typically parametrised in terms of the near-bed velocity $\boldsymbol{u}_b$ (which is usually taken as the flow velocity at the bottom of the water column). Friction formulations are generally derived from the law of the wall, assuming a balance between turbulent production and dissipation, leading to quadratic expressions in the near-bed velocity $\boldsymbol{u}_b$ with the bed roughness often parametrised using a roughness scale z_0 (see, e.g., Vreugdenhil, 1994; Pope, 2000). To simplify the analysis, this formulation is often linearised to obtain the associated linearised

* Corresponding author.
E-mail address: M.P.Rozendaal@tudelft.nl (M.P. Rozendaal).

https://doi.org/10.1016/j.ocemod.2024.102330
Received 25 August 2023; Received in revised form 18 January 2024; Accepted 18 January 2024
Available online 24 January 2024

friction law (see, e.g., Hulscher, 1996):

$$\frac{\boldsymbol{\tau}_b}{\rho} = s_f \boldsymbol{u}_b. \tag{1}$$

Here, ρ is the density of water and $s_f(x, y)$ (in m/s) a partial slip parameter, which parametrises the bed roughness and the local velocity scale. In depth-averaged models, the bed shear stress must be parametrised in terms of the depth-averaged velocity $\overline{\boldsymbol{u}}$. When considering a linearised bed shear stress in 2DH models, this traditionally results in a relation of the form (see, e.g., Schramkowski et al., 2002):

$$\frac{\boldsymbol{\tau}_b}{\rho} = r\overline{\boldsymbol{u}}, \tag{2}$$

with bottom friction coefficient $r(x, y)$ (in m/s), which parametrises the bed roughness and the local near-bed velocity scale. The partial slip parameter s_f and the bottom roughness coefficient r are sometimes reformulated in terms of other friction coefficients (e.g., Chézy, Manning) or in terms of a velocity scale using, for example, Lorentz linearisation (see, e.g., Vreugdenhil, 1994; Dingemans, 1997).

There is ample evidence in the literature that there are differences between the water motion computed using 3D and 2DH models (see, e.g., Marinone, 2000; Glock et al., 2019). Three different aspects have been identified that cause the 3D and 2DH bed shear stresses to differ. Firstly, a theoretical analysis was performed by Vreugdenhil (1994) to verify the validity of the parametrisation of the velocity near the bed in terms of the depth-averaged velocity in a highly simplified two-dimensional vertical (2DV) model for which simple analytic solutions exist. He found that there is a phase difference between the velocity near the bed and the depth-averaged velocity for harmonic signals. This phase difference was also observed earlier by, e.g., Mofjeld (1980), Prandle (1982), Soulsby (1983). Secondly, Mofjeld (1980) has compared 3D and 2DH Kelvin wave solutions on the continental shelf and found subtle differences. One of the reasons he mentions for this discrepancy is that the parametrisation of the bed shear stress in terms of the depth-averaged velocity assumes that it acts in the same direction as the depth-averaged velocity. However, the rotation of earth causes veering in the bottom boundary layer such that the bed shear stress may not point in the same direction as the depth-averaged velocity. An example of this veering was provided by Soulsby (1981), showing observations where the bottom current was directed 48° clockwise of the surface current. Thirdly, Zielke (1966) considered the friction formulation for transient pipe flow. He derived a frequency-dependent friction formulation to exactly parametrise the wall shear stress in a cross-sectionally-averaged model and showed that this formulation better matched the observed resonance behaviour than a friction formulation that does not depend on the frequency.

In summary, 3D and 2DH friction may differ because the near-bed and depth-averaged velocity may differ in direction and magnitude due to 1) phase differences, 2) Coriolis deflection and 3) frequency dependency. However, it remains unclear how to consistently parametrise the effect of the depth, including these three aspects, in a 2DH model such that the same depth-averaged dynamics are described as in the corresponding 3D model. Restricting ourselves to barotropic models, the main aim of this contribution is to derive a consistent parametrisation of 2DH bed shear stress such that the same depth-averaged dynamics are obtained as in the corresponding 3D model.

The structure of this paper is as follows. In Section 2, the linearised 3D and corresponding 2DH model are presented. In Section 3, the 3D friction formulation is derived for a single harmonic component, a physical interpretation is provided and the result is extend to general time signals. In Section 4, we present a parameter sensitivity analysis of the 3D friction formulation, show the importance of the 3D friction formulation in a narrow well-mixed estuary and use the amplification plane to explain the observed resonance behaviour. The discussion in Section 5 illustrates that 3D friction is inherently different than 2DH friction and Section 6 provides a summary of the main findings.

2. Model formulation

2.1. The 3D hydrodynamic equations

The linearised incompressible three-dimensional Reynolds-averaged shallow water equations are often used to describe the water motion in shelf seas and estuaries (Mofjeld, 1980; Winant, 2007). In these equations, the hydrostatic balance, the Boussinesq approximation, the eddy viscosity formulation and the f-plane approximation are used and the non-linearities have been linearised or neglected using scaling arguments. Neglecting density gradients, these equations read

$$\begin{cases} \zeta_t + \left(\int_{-H}^{R} u\,dz\right)_x + \left(\int_{-H}^{R} v\,dz\right)_y = 0, \\ u_t - fv = -g\zeta_x + \left(A_v u_z\right)_z, \\ v_t + fu = -g\zeta_y + \left(A_v v_z\right)_z, \end{cases} \tag{3}$$

where, $\zeta(x, y, t)$ is the free surface, $\boldsymbol{u}(x, y, z, t) = (u, v)^T$ represents the horizontal velocity vector with T denoting the transpose, x, y and z are the three Cartesian coordinates in a right-handed coordinate system with z pointing upwards, t is time, f the Coriolis parameter, g the acceleration of gravity, $R(x, y)$ a subtidal surface level (Dijkstra, 2019), $-H(x, y)$ is the bed level and $A_v(x, y)$ is the vertical eddy viscosity. It is assumed that the eddy viscosity parameter A_v is uniform in the vertical dimension[1]. The subscripts x, y, z and t denote taking the partial derivative with respect to these variables. The first equation is the depth-integrated continuity equation and the last two equations describe the conservation of momentum in the two horizontal dimensions. The vertical flow velocity $w(x, y, z, t)$ has been eliminated from the model by integrating the 3D continuity equation over depth and using the kinematic boundary conditions imposed at the free surface and bed. Therefore, only dynamic boundary conditions need to be imposed at these boundaries.

At the free surface, which in the linearised formulation is found at the subtidal reference level $z = R$, a no-stress boundary condition is imposed:

$$A_v \boldsymbol{u}_z = \boldsymbol{0}, \qquad \text{at} \quad z = R, \tag{4}$$

whereas at the bottom, the bed shear stress is imposed through the partial-slip condition (see, e.g, Eq. (1) or Schramkowski and De Swart, 2002):

$$\frac{\boldsymbol{\tau}_b}{\rho} \equiv A_v \boldsymbol{u}_z = s_f \boldsymbol{u}_b, \quad \text{at} \quad z = -H. \tag{5}$$

Here, $s_f(x, y)$ is the partial-slip coefficient and the near-bed velocity is defined as $\boldsymbol{u}_b = \boldsymbol{u}$ at $z = -H$. For these boundary conditions to remain valid, it is assumed that the changes in the subtidal surface level and bed are gradual throughout the domain, i.e., the magnitude of their gradients is assumed to remain small.

At the open boundaries, the free surface level is imposed:

$$\zeta = A(x, y, t), \qquad \text{at} \quad \partial\Omega_{\text{open}}, \tag{6}$$

and at the closed boundaries, a no-transport condition is prescribed:

$$\left(\int_{-H}^{R} \boldsymbol{u}\,dz\right) \cdot \boldsymbol{n} = 0, \quad \text{at} \quad \partial\Omega_{\text{closed}}. \tag{7}$$

Here, $\boldsymbol{n}$ is the outward pointing unit normal.

[1] The methods described in this paper can be extended to vertically varying A_v.

2.2. The 2DH hydrodynamic equations

To obtain the 2DH hydrodynamic equations, the 3D momentum Eqs. (3) are integrated over the depth and the no-stress and partial-slip boundary conditions (4), (5) are used, whereas the depth-integrated continuity Eq. (3) can be expressed directly in terms of the depth-averaged velocity components $\overline{u}$, $\overline{v}$. Here, the bar $\overline{[\cdot]}$ denotes the depth-averaging operator defined as

$$\overline{[\cdot]} = \frac{1}{D}\int_{-H}^{R} [\cdot]\, dz, \tag{8}$$

with $D(x,y) = H(x,y) + R(x,y)$ denoting the local water depth. The depth-averaged shallow water equations solving for the free surface $\zeta(x,y,t)$ and the depth-averaged velocity components $\overline{u}(x,y,t)$, $\overline{v}(x,y,t)$ read

$$\begin{cases} \zeta_t + \left(D\overline{u}\right)_x + \left(D\overline{v}\right)_y = 0, \\ \overline{u}_t - f\overline{v} = -g\zeta_x - \dfrac{1}{D}s_f u_b, \\ \overline{v}_t + f\overline{u} = -g\zeta_y - \dfrac{1}{D}s_f v_b. \end{cases} \tag{9}$$

At the open boundaries, Eq. (6) still holds and at the closed boundaries, Eq. (7) is expressed in terms of the depth-averaged velocity, yielding a no-transport boundary condition for the depth-averaged velocity:

$$\overline{\boldsymbol{u}} \cdot \boldsymbol{n} = 0, \quad \text{at} \quad \partial\Omega_{\text{closed}}, \tag{10}$$

with $\boldsymbol{n}$ is the outward pointing unit normal vector.

2.2.1. 2DH closure problem

To obtain a closed system of equations, the unresolved near-bed velocity components u_b, v_b still need to be parametrised in terms of the resolved depth-averaged velocity components $\overline{u}$, $\overline{v}$. To this end, we assume there exists a linear operator $\boldsymbol{\mathcal{L}}$ such that the bed shear stress of the 3D model is exactly reproduced in the 2DH model:

$$\frac{\boldsymbol{\tau}_b}{\rho} = s_f \boldsymbol{u}_b = \boldsymbol{\mathcal{L}}\left\{\overline{\boldsymbol{u}}\right\}. \tag{11}$$

Another interpretation of the linear operator $\boldsymbol{\mathcal{L}}$ is that it shows, up to a factor s_f, how to parametrise the near-bed velocity $\boldsymbol{u}_b$ in terms of the depth-averaged velocity $\overline{\boldsymbol{u}}$.

3. The relationship between linearised 3D and 2DH models

In this section, a systematic derivation of the operator $\boldsymbol{\mathcal{L}}$ is presented such that 3D and 2DH models describe the same depth-averaged dynamics. In Section 3.1, the derivation for harmonic signals is shown and in Section 3.2 the result for general time signals is given. The operator $\boldsymbol{\mathcal{L}}$ is fully analytical in both cases and the harmonic case provides an intuitive way to interpret the results. This case is discussed in detail.

3.1. The equivalent 2DH equations for harmonic signals

We solve for the water motion that is in dynamic equilibrium with the forcing, thereby neglecting any transients. For the harmonic case, we assume that the forcing consists of a single tidal constituent with angular frequency ω. Since the 2DH hydrodynamic equations are linear, it follows that the solution has the same time dependency as the forcing. Thus we may expand the free surface, depth-averaged and near-bed velocity components as follows

$$\begin{bmatrix} \zeta \\ \overline{u} \\ \overline{v} \\ u_b \\ v_b \end{bmatrix}(x,y,t) = \Re\mathfrak{e}\left\{ \begin{bmatrix} Z \\ \overline{U} \\ \overline{V} \\ U_b \\ V_b \end{bmatrix}(x,y;\omega)\, \exp(i\omega t) \right\}. \tag{12}$$

Here, i is the imaginary unit, Z the complex free surface elevation, $\overline{U}$, $\overline{V}$ are the complex depth-averaged velocity components, U_b, V_b the complex near-bed velocity components and '$;\omega$' denotes that ω is treated as a parameter rather than a variable.

Substituting these expansions into the 2DH Eqs. (9) results in

$$\begin{cases} i\omega Z + \left(D\overline{U}\right)_x + \left(D\overline{V}\right)_y = 0, \\ i\omega\overline{U} - f\overline{V} = -gZ_x - \dfrac{1}{D}s_f U_b, \\ i\omega\overline{V} + f\overline{U} = -gZ_y - \dfrac{1}{D}s_f V_b. \end{cases} \tag{13}$$

A depth-averaged model cannot explicitly resolve the bed shear stress $s_f \boldsymbol{U}_b$, as it only resolves the depth-averaged velocity $\overline{\boldsymbol{U}}$. To determine the relationship between $\boldsymbol{U}_b$ and $\overline{\boldsymbol{U}}$, the associated 3D model (3) with harmonic forcing is used. Winant (2007) and Kumar et al. (2016) provide analytical solutions for the vertical structure of these 3D hydrodynamic equations. This allows for an exact parametrisation of the near-bed velocity in terms of the depth-averaged velocity. The resulting exact bed shear stress parametrisation in the frequency domain reads

$$s_f \boldsymbol{U}_b(x,y;\omega) = \mathbf{R}^{3D}(x,y;\omega)\,\overline{\boldsymbol{U}}(x,y;\omega). \tag{14}$$

This equation is the complex counterpart of Eq. (11). The entries of the complex-valued 3D friction matrix can be expressed as

$$\mathbf{R}^{3D}(x,y;\omega) = s_f \begin{bmatrix} r_1 e^{i\varphi_1} & -r_2 e^{i\varphi_2} \\ r_2 e^{i\varphi_2} & r_1 e^{i\varphi_1} \end{bmatrix}. \tag{15}$$

Explicit analytical expressions of amplitudes $r_{1,2}$ and phases $\varphi_{1,2}$ are derived in Appendix A. The 3D friction matrix can also be expressed in terms of parameters that have a geometric interpretation. The geometric form reads

$$\mathbf{R}^{3D}(x,y;\omega) = s_f\, r_a e^{i\varphi_a}\left(\mathbf{Q}(\varphi_d) + i r_r \mathbf{Q}(\varphi_d - \pi/2)\right). \tag{16}$$

Here, r_a is the average amplitude, r_r the amplitude ratio, φ_a the average phase, φ_d the phase deviation and $\mathbf{Q}(\varphi_d)$ is the 2 by 2 anticlockwise rotation matrix through the angle φ_d:

$$\mathbf{Q}(\varphi_d) = \begin{bmatrix} \cos\varphi_d & -\sin\varphi_d \\ \sin\varphi_d & \cos\varphi_d \end{bmatrix}.$$

Analytical expressions for the amplitudes r_a, r_r and phases φ_a, φ_d are given in Supplementary Material S1 and a geometrical interpretation is provided in Fig. 1. In case the Coriolis parameter vanishes, the amplitude ratio r_r and phase deviation φ_d vanish, reducing the 3D friction formulation to

$$\mathbf{R}^{3D}(x,y;\omega) = s_f\, r_a e^{i\varphi_a}\, \mathbf{I}_2, \tag{17}$$

with $\mathbf{I}_2$ the 2 by 2 identity matrix.

The amplitudes and phases depend on five nondimensional numbers:

$$\mathcal{A}(x,y) = \frac{A_v}{s_f D}, \quad \mathrm{Stk}_{\pm}(x,y;\omega) = \frac{1}{D}\sqrt{\frac{A_v}{|\omega \pm f|}}, \quad \mathcal{P}_{\pm} = \mathrm{sign}(\omega \pm f). \tag{18}$$

The non-dimensional parameter $\mathcal{A}$ is the ratio between the vertical eddy viscosity A_v and the product of the partial-slip parameter s_f and the depth D. This non-dimensional parameter may be derived from the partial-slip boundary condition. The non-dimensional parameters $\mathrm{Stk}_{\pm}$ are modifications of the classical Stokes number Stk with ω replaced by $\omega \pm f$ and omitting a factor $\sqrt{2}$ yielding the Stokes plus Stk_+ and the Stokes min Stk_- numbers (Souza, 2013). The nondimensional numbers $\mathcal{P}_{\pm}$ only depend on the sign of the frequency scale $\omega \pm f$ and are discretely valued, taking only the values −1, 0 and 1.

To interpret the 3D friction formulation, we transform the 2DH equations back to the time domain. This yields the equivalent 2DH equations for harmonic signals:

$$\begin{cases} \zeta_t + \left(D\overline{u}\right)_x + \left(D\overline{v}\right)_y = 0, \\ \overline{u}_t - f\overline{v} = -g\zeta_x - \dfrac{1}{D}s_f\left[r_1\overline{u}(t+t_1) - r_2\overline{v}(t+t_2)\right], \\ \overline{v}_t + f\overline{u} = -g\zeta_y - \dfrac{1}{D}s_f\left[r_1\overline{v}(t+t_1) + r_2\overline{u}(t+t_2)\right], \end{cases} \tag{19}$$

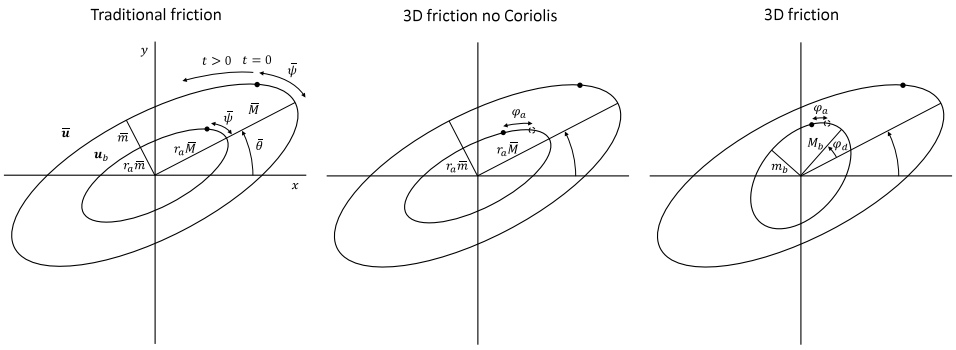

Fig. 1. Graphical representation of the relationship between the depth-averaged velocity $\overline{\boldsymbol{u}}$ and the near-bed velocity $\boldsymbol{u}_b$ for the traditional, 3D friction no Coriolis and 3D friction formulation.

with the boundary conditions given by Eqs. (6) and (10) and the time shift t_j for $j = 1, 2$ given by

$$t_j = \frac{\varphi_j}{\omega}. \tag{20}$$

Thus for harmonic signals, the linear operator $\boldsymbol{\mathcal{L}}$ is given by

$$\boldsymbol{\mathcal{L}}\left\{\overline{\boldsymbol{u}}\right\} = s_f \begin{bmatrix} r_1\overline{u}(t+t_1) - r_2\overline{v}(t+t_2) \\ r_1\overline{v}(t+t_1) + r_2\overline{u}(t+t_2) \end{bmatrix}. \tag{21}$$

No additional assumptions have been made during the derivation of the linear operator $\boldsymbol{\mathcal{L}}$ for harmonic signals. This means that this parametrisation of the bed shear stress for 2DH models is exact, provided the made assumptions hold. Thus, the depth-averaged and depth-resolving model describe the exact same water levels and depth-averaged velocities. This is further elaborated upon in Section 4.3, where an idealised well-mixed estuary is considered.

3.1.1. Interpretation of the 3D friction formulation using the tidal ellipse

To illustrate the differences between the traditional and the 3D friction formulation for 2DH models, we introduce the linear operator $\boldsymbol{\mathcal{L}}_{\text{traditional}}$ that corresponds to the traditional friction formulation, see Eq. (2):

$$\boldsymbol{\mathcal{L}}_{\text{traditional}}\left\{\overline{\boldsymbol{u}}\right\} = s_f r_a \begin{bmatrix} \overline{u}(t) \\ \overline{v}(t) \end{bmatrix}. \tag{22}$$

Here, we have factored the 2DH bottom friction coefficient as $r = s_f r_a$ with r_a a non-dimensional scaling parameter, to facilitate the comparison with the 3D friction formulation given by Eq. (21) and the complex geometric form given by Eq. (17).

Comparing $\boldsymbol{\mathcal{L}}$ with $\boldsymbol{\mathcal{L}}_{\text{traditional}}$ shows that each component of the 3D friction formulation depends, in general, on both depth-averaged velocity components that are both scaled and time (or phase) shifted with respect to the instantaneous depth-averaged velocity. This Cartesian form of the 3D friction formulation may be understood using Jones calculus, which is typically used to describe the elliptical polarisation of light (see, e.g., Chekhova and Banzer, 2021).

To give a more geometrical explanation, we use the fact that the velocity vectors trace an ellipse over the tidal cycle (which may collapse into a one-dimensional line segment if the minor axis vanishes) (see, e.g., Souza and Simpson, 1996). Thus both the depth-averaged and near-bed velocity trace out an ellipse. Using the 3D friction formulation, we are able to relate the near-bed tidal ellipse parameters to the depth-averaged tidal ellipse parameters. Given the depth-averaged tidal ellipse parameters, this describes how the near-bed tidal ellipse changes as a consequence of the 3D friction formulation.

We describe a tidal ellipse using five parameters: the magnitude of the semi-major axis M, the signed magnitude of the semi-minor axis m, the orientation of the ellipse θ, the phase of the ellipse ψ and the signed ellipticity ε (see, e.g., Souza and Simpson, 1996). The depth-averaged tidal ellipse parameters are denoted with $\overline{[\cdot]}$ and the near-bed tidal ellipse parameters with $[\cdot]_b$. The near-bed tidal ellipse parameters

Table 1
Definition of the near-bed tidal ellipse parameters M_b, m_b, θ_b, ψ_b and ε_b under the traditional and 3D friction formulation. The parameters $\overline{M}$, $\overline{m}$, $\overline{\theta}$, $\overline{\psi}$ and $\overline{\varepsilon}$ are the tidal ellipse parameters of the depth-averaged velocity and the parameters r_a, r_r, φ_a and φ_d follow from the (3D) friction formulation.

	M_b	m_b	θ_b	ψ_b	ε_b
Traditional	$\overline{M} r_a$	$\overline{m} r_a$	$\overline{\theta}$	$\overline{\psi}$	$\overline{\varepsilon}$
3D No Coriolis	$\overline{M} r_a$	$\overline{m} r_a$	$\overline{\theta}$	$\overline{\psi} - \varphi_a$	$\overline{\varepsilon}$
3D Coriolis	$\overline{M} r_a(1 + \overline{\varepsilon} r_r)$	$\overline{M} r_a(\overline{\varepsilon} + r_r)$	$\overline{\theta} + \varphi_d$	$\overline{\psi} - \varphi_a$	$\frac{\overline{\varepsilon} + r_r}{1 + \overline{\varepsilon} r_r}$

can be expressed in terms of the depth-averaged tidal ellipse parameters and four dimensionless variables that follow from the 3D friction formulation: the average amplitude r_a, amplitude ratio r_r, average phase φ_a and phase deviation φ_d, see Table 1 and Supplementary Material S1 for details.

In Fig. 1, the relationship between the depth-averaged velocity and the near-bed velocity is depicted for the traditional friction formulation (left panel), 3D no Coriolis formulation (middle panel) and the full 3D friction formulation (right panel). Below, these cases are discussed:

- The traditional formulation implicitly assumes that the near-bed velocity points in the same direction as the depth-averaged velocity. Using the scaling factor r_a, only the magnitude of the near-bed velocity can be altered. The result is that the near-bed tidal ellipse is a scaled version of the depth-averaged tidal ellipse.
- The 3D friction formulation in absence of the Coriolis force shows that the near-bed velocity still follows a scaled version of the depth-averaged ellipse, but the near-bed velocity does not necessarily point in the same direction as the depth-averaged velocity due to the possible existence of the phase shift φ_a, which is generally positive. This phase shift causes the near-bed velocity to lead the depth-averaged velocity. This phase lead can be explained as follows. The near-bed velocity is smaller than the velocity higher in the water column due to bottom friction. The water level gradient generates a depth-uniform pressure gradient. The pressure gradient acts on all fluid layers equally and produces a velocity pointing in the same direction as this gradient, more rapidly in the slower-moving layers near the bed than in the layers higher in the water column (Van Rijn, 2010; Batchelor, 1967, p. 355). This causes the near-bed velocity to lead the depth-averaged velocity.
- For the full 3D friction formulation, the near-bed velocity does not point in the depth-averaged direction due to a φ_d rotation of the semi-major axis of the near-bed ellipse, a φ_a phase shift of the near-bed ellipse and an alteration of the ellipticity of the near-bed tidal ellipse ε_b due to non-zero amplitude ratio r_r (see the right panel of Fig. 1). These effects are caused by the interaction between the Coriolis force and the vertical dimension. The Coriolis force acts perpendicular to the current velocity (with

the sign dependent on the hemisphere) and it causes the velocity to rotate over the vertical. A classical example for steady currents is the Ekman spiral (see, e.g., Cushman-Roisin and Beckers, 2009). To conclude, under the 3D friction formulation, the near-bed tidal ellipse is generally rotated, deformed and phase shifted with respect to the depth-averaged tidal ellipse.

The 3D friction formulation depends on the five nondimensional parameters given by Eq. (18), which in turn depend on the tidal angular frequency ω. While the above derivation assumed one harmonic constituent, the derivation follows analogously when resolving multiple harmonic components. For each harmonic, the same formulation is found but with ω replaced by the considered frequency, see Supplementary Material S6 for details.

A direct consequence of the ω dependence is that within a harmonic 2DH model, each resolved frequency component experiences a different effective friction parameter, whereas using the traditional friction formulation a single friction parameter is used for all resolved frequency components, see Supplementary Material S6 for details. The need for multiple effective friction parameters is explained by the fact that for each frequency component ω, a different vertical profile is established in the 3D model, thereby changing the relationship between the depth-averaged and near-bed velocity and requiring different friction parameters.

3.2. The 3D friction formulation for general time signals

The friction formulation can be generalised to arbitrary (i.e, non-harmonic) time signals using the Fourier transform. The derivation is presented in Supplementary Material S4. The resulting convolutional 3D friction formulation is given by

$$\mathcal{L}\left\{\overline{\boldsymbol{u}}\right\} = s_f\left(\overline{\boldsymbol{u}}(t) - \sigma\left(g(\sigma t)\,\mathbf{Q}^T(ft) * \overline{\boldsymbol{u}}\right)(t)\right). \tag{23}$$

Here, $\sigma = A_v/D^2$ is a vertical frequency scale, $\mathbf{Q}^T(ft)$ is the 2×2 *clockwise* rotation matrix over an angle ft with f the Coriolis parameter and $g(t)$ is a kernel that describes the depth-dependent behaviour and is given by Eq. (S5.22). The symbol $*$ denotes the convolution operator and is defined for functions $p(t)$ and $q(t)$ as

$$\left(p * q\right)(t) = \int_{-\infty}^{\infty} p(\tau)q(t-\tau)\,d\tau. \tag{24}$$

This definition of the convolution operator remains valid even when the convolution between a matrix and vector is considered. Using linearity, it follows that this is the same as applying the convolution operator to each element of the matrix vector product individually.

The convolutional 3D friction formulation may be expanded to find the following form:

$$\mathcal{L}\left\{\overline{\boldsymbol{u}}\right\} = s_f\begin{bmatrix}\overline{u}(t) - \sigma\left(h_1 * \overline{u}\right)(t) - \sigma\left(h_2 * \overline{v}\right)(t)\\ \overline{v}(t) + \sigma\left(h_2 * \overline{u}\right)(t) - \sigma\left(h_1 * \overline{v}\right)(t)\end{bmatrix}. \tag{25}$$

Here, $h_1(t)$, $h_2(t)$ are known frictional convolution kernels and are defined in Eq. (S5.21). All friction kernels $h_1(t)$, $h_2(t)$ and $g(\sigma t)\,\mathbf{Q}^T(ft)$ are causal, meaning that they do not depend on the future of the signal. Mathematically, this condition requires that the friction kernels vanish for negative time values (i.e., they must equal 0 for $t < 0$).

The convolutional 3D friction formulation (23) prescribes an instantaneous friction value based on the instantaneous depth-averaged velocity and its history (weighted according to the convolution kernel $g(\sigma t)\,\mathbf{Q}^T(ft)$), thereby generalising the result for a single harmonic component where 3D friction depends on the time shifted velocity. The expanded form (25) illustrates the dependency of the velocity components on the history kernels h_1 and h_2.

Comparing the convolutional friction formulation with the traditional friction formulation shows that the first term is the same as the traditional friction formulation with $r_a = 1$, however, the second term cannot be captured using the traditional friction formulation as it introduces history dependent behaviour. This term is required to fully capture the 3D effects within a 2DH model.

4. Results

In this section, an interpretation of the 3D friction formulation is presented and the implications of this friction formulation are investigated.

4.1. Sensitivity of the tidal ellipse parameters of the 3D friction formulation — no coriolis

We first concentrate on the harmonic case with no Coriolis force: $f = 0$. In this case the parameters describing the tidal ellipse for the 3D friction formulation (21) simplify (see Appendix A for analytic expressions). Since $\omega > 0$, it follows that $\mathcal{P}_{\pm} = 1$. Furthermore, since $f = 0$, the Stokes numbers Stk_+, Stk_- reduce to the classical Stokes number Stk. As a result, the average amplitude r_a and average phase φ_a only depend on the nondimensional parameters $\mathcal{A}$ and Stk, and the amplitude ratio r_r and phase deviation φ_d vanish. The parameters r_a and φ_a may be interpreted as the scaling and phase shift between the near-bed velocity $\boldsymbol{u}_b$ and the depth-averaged velocity $\overline{\boldsymbol{u}}$, respectively, as illustrated the middle panel of Fig. 1.

In Fig. 2, contour plots of the average amplitude r_a and average phase φ_a are shown as functions of the nondimensional parameters $\mathcal{A}$ and Stk. The nondimensional amplitude r_a (left panel) ranges from 0 to 1. At approximately $\mathrm{Stk} = 1$, where the frictional depth is comparable in magnitude to the local depth, the contour lines saturate and larger values of Stk do not significantly influence the value of the amplitude any more. On the other hand in the region $\mathrm{Stk} < 1$, both parameters influence the amplitude. The amplitude is approximately constant along the diagonal line segments where Stk is proportional to $\mathcal{A}$. The phase shift φ_a (right panel) ranges from 0 to 45° (i.e., no phase shift for $\varphi_a = 0$ to a time advancement of 1/8 of the wave period for $\varphi_a = 45°$). For large Stokes numbers $\mathrm{Stk} > 1$, the phase shift is very small. For smaller Stokes numbers, $\mathrm{Stk} < 1$, a region appears where the phase shift becomes significant for small $\mathcal{A}$. For larger values of $\mathcal{A}$, the phase shift decreases to zero again. The sloped contour lines approximately occur when Stk is proportional to $\mathcal{A}$.

To understand these results physically, we consider two (limit) cases for the Stokes number. We consider very large Stokes numbers ($\mathrm{Stk} \gg 1$), where the frictional depth occupies the whole water column, and very small Stokes numbers ($\mathrm{Stk} \ll 1$), where the frictional depth occupies only a small part of the water column near the bed.

- For large Stokes numbers ($\mathrm{Stk} \gg 1$), the nondimensional parameter $\mathcal{A}$ fully determines the behaviour of the average amplitude r_a (left panel of Fig. 2). For small $\mathcal{A} \ll 1$, the partial-slip boundary condition behaves as a no-slip boundary condition, resulting in a near-zero velocity at the bed. As a consequence, the average amplitude r_a is approximately zero as well, as it may be interpreted as the scaling between the near-bed and depth-averaged velocity. Conversely, for large $\mathcal{A} \gg 1$, the partial-slip boundary condition behaves as a free-slip boundary condition, so the near-bed velocity is approximately equal to the free stream velocity. This causes the velocity profile to be approximately vertically uniform and the average amplitude r_a to be close to unity. In between these two limits, a smooth transition is found where the full partial-slip condition must be taken into account. Furthermore, since the frictional depth occupies the whole water column ($\mathrm{Stk} \gg 1$), the phase difference between the near-bed velocity and the depth-averaged velocity remains minor (right panel).
- For small Stokes numbers ($\mathrm{Stk} \ll 1$), the effect of the bottom boundary condition is confined to a small region near the bed, a boundary layer. The thickness of this boundary layer scales with the Stokes number Stk. Rescaling the partial slip condition by the

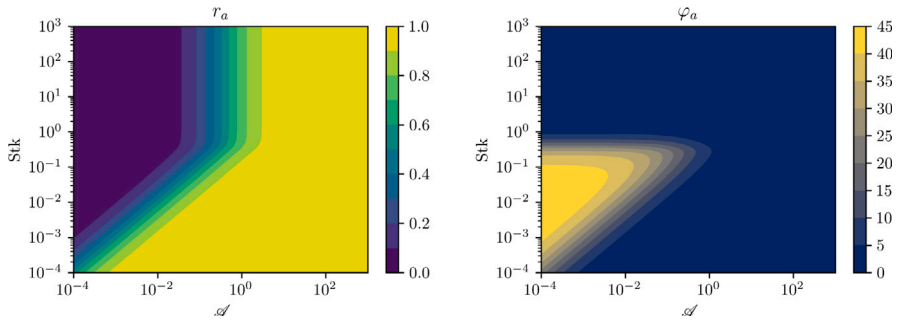

Fig. 2. Contour plots of the nondimensional average amplitude r_a and average phase φ_a (in degrees) as functions of the nondimensional parameters $\mathcal{A}$ and Stk for $\omega > 0$.

length scale of the boundary layer $\tilde{z} = (z+1)/\mathrm{Stk}$ yields (see, Supplementary Material S2)

$$\frac{\mathcal{A}}{\mathrm{Stk}}\boldsymbol{u}_{\tilde{z}} = \boldsymbol{u}_b. \tag{26}$$

Rather than comparing the magnitude of $\mathcal{A}$ to unity as we did for large Stk, we instead compare the magnitude of $\mathcal{A}$ to the magnitude of Stk.

Focussing on the average amplitude r_a. This means that for $\mathcal{A} \ll \mathrm{Stk}$, the no-slip balance dominates, resulting in the slanted dark blue region for r_a (left panel of Fig. 2). Conversely, for $\mathcal{A} \gg \mathrm{Stk}$, the free-slip balance dominates, yielding the slanted yellow region for r_a. For intermediate values $\mathcal{A} \approx \mathrm{Stk}$, a transition region is found.

Next, we consider the average phase φ_a. For $\mathcal{A} \gg \mathrm{Stk}$, the free-slip balance dominates causing a uniform velocity profile over the whole depth and the disappearance of the boundary layer. Hence, there is almost no phase shift in this case, as depicted with the slanted dark blue region in the right panel of Fig. 2. For $\mathcal{A} \ll \mathrm{Stk}$, a real boundary layer is formed where the velocity rapidly decreases from the free stream velocity at the top of the boundary layer to the much smaller velocity near the bed. The dynamics in the boundary layer are such that the velocity across the boundary layer attains at most a phase shift of 45° (see, e.g., Batchelor, 1967, p. 355). This is shown with the slanted light region on the right panel of Fig. 2.

Using a boundary layer analysis for small Stokes numbers ($\mathrm{Stk} \ll 1$), it can be shown that the average phase shift φ_a is indeed entirely due to the phase shift attained in the boundary layer, see Supplementary Material S2, and can be expressed as

$$\varphi_a = \arctan\left(\frac{1}{1+\sqrt{2}\mathcal{A}/\mathrm{Stk}}\right). \tag{27}$$

4.2. Sensitivity of the tidal ellipse parameters of the 3D friction formulation — including coriolis

We consider the sensitivity of the tidal ellipse parameters of the 3D friction formulation under the Coriolis force, i.e, $f \neq 0$. We assume that $|f| < \omega$ such that $\mathcal{P}_\pm = 1$.

In Fig. 3, the average amplitude r_a, amplitude ratio r_r, average phase φ_a and phase deviation φ_d are shown as functions of the nondimensional parameters Stk_+ and Stk_- for $\mathcal{A} = 10^{-2}$. The dashed diagonal lines, where $\mathrm{Stk}_- = \mathrm{Stk}_+ = \mathrm{Stk}$, correspond to the no-Coriolis case. Along these diagonal lines, the average amplitude r_a and average phase φ_a correspond to the vertical lines of the no-Coriolis case depicted in Fig. 2 with $\mathcal{A} = 10^{-2}$.

The top left panel of Fig. 3 shows the average amplitude r_a, which is largest for small $\mathrm{Stk}_\pm$. When increasing either Stk_+ or Stk_-, the amplitude seems to eventually plateau to a constant value. However, if we increase both $\mathrm{Stk}_\pm$ the amplitude r_a goes to zero. The top right panel of Fig. 3, displays the phase shift φ_a. For $\mathcal{A} = 10^{-2}$, it attains a maximum near $\mathrm{Stk}_\pm = 10^{-1}$. Increasing or decreasing either Stk_+ or Stk_- decreases this value until again a plateau reached. Changing both $\mathrm{Stk}_\pm$, the phase shift φ_a may go to zero again. The lower left panel of Fig. 3 displays the amplitude ratio r_r. Along the diagonal line r_r vanishes and in the small Stk_+ large Stk_- regime (upper left corner), the parameter attains a maximum, conversely in the large Stk_+ small Stk_- regime (lower right corner) it attains a minimum. The lower right panel of Fig. 3 shows the phase deviation φ_d. Along the diagonal φ_d vanishes and along the lines of constant $\mathrm{Stk}_\pm = 10^{-1}$, it attains its maximum and minimum values.

The phase shift φ_a is generally positively valued, whereas φ_d can be both positive or negative, indicating that the angle the semi-major axis of the near-bed tidal ellipse makes with the semi-major axis of the depth-averaged tidal ellipse can be both to the left and to the right depending on the sign of φ_d.

The ellipticity of the near-bed tidal ellipse can be recovered by considering the value of r_r and the ellipticity of the depth-averaged tidal ellipse $\bar{\varepsilon}$. For $r_r = 1$, the near-bed tidal ellipse becomes an anticlockwise rotating circle since $\varepsilon_b = 1$, whereas for $r_r = -1$, a clockwise rotating circle is found. If the depth-averaged velocity describes a line, $\bar{\varepsilon} = 0$, then the ellipticity of the near-bed tidal ellipse is equal to $\varepsilon_b = r_r$. The near-bed tidal ellipse describes a line for $\varepsilon_b = 0$ which implies that $r_r = -\bar{\varepsilon}$.

4.3. Example: A narrow well-mixed estuary

To illustrate the effect of the new 3D friction formulation on the barotropic water motion, a narrow and well-mixed rectangular estuary is considered. The parameters are uniform in the along- and across-channel direction and the Coriolis force is neglected. The estuary is forced at the seaward side with a laterally uniform M_2 tidal constituent and the lateral and landward sides are closed. The parameter values used can be found in Table 2. The water motion within this estuary is computed using four different models: a 3D model, a 2DH model without friction, a 2DH model where the traditional friction parameter r_a is chosen such that the best possible fit with the 3D model is achieved and a 2DH model where the 3D friction parameters (r_a, φ_a) are computed using the 3D friction formulation, see Table 3. We define the best fit as the function that minimises the error in the L^2-norm.

In Fig. 4, the amplitude and phase of the water level of the M_2 tidal constituent are shown along the longitudinal axis of the estuary. The water motion computed using the 3D model (blue), 2DH best fit (green) and 2DH 3D friction (red) have a progressive nature near the mouth and transition into a standing wave near the landward end, whereas the water motion computed using the 2DH frictionless model (orange) is a pure standing wave.

This figure shows that the results obtained using the 3D model and the 2DH model using the 3D friction formulation are identical. Comparing the 2DH best fit with the 3D model shows a difference in amplitude of approximately 60 cm at the landward end and a difference in phase of approximately 1°.

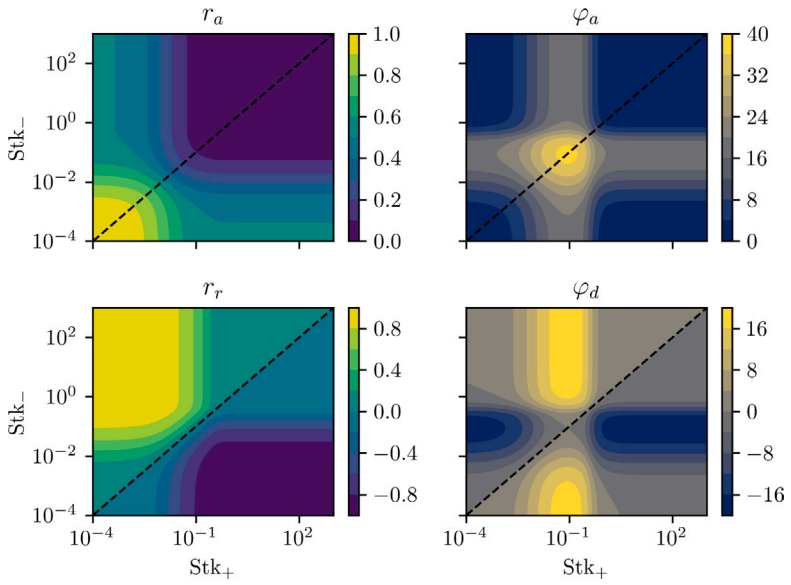

Fig. 3. Contour plots of the nondimensional amplitudes r_a, r_r and phases φ_a, φ_d (in degrees) as functions of the nondimensional parameters Stk_+ and Stk_- for the nondimensional parameters $\mathcal{A} = 10^{-2}$ and $\mathcal{P}_\pm = 1$.

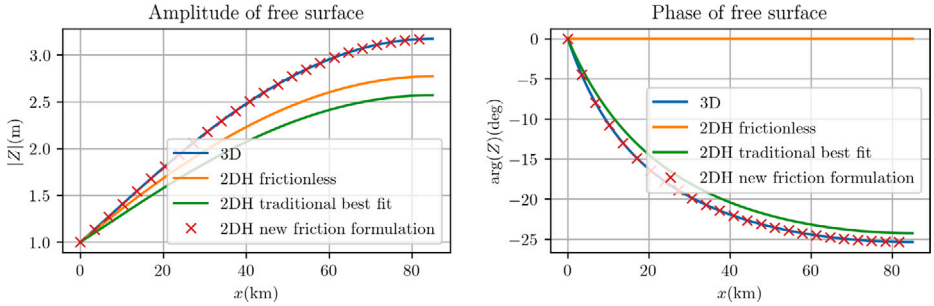

Fig. 4. Amplitude and phase of the water level of the M_2 tidal constituent as function of the distance from the estuarine mouth. The results are computed using four different models.

Table 2
The parameters used in the narrow well-mixed estuary example.

		Parameters	
Geometry	L	Length of estuary	85 km
	B	Width of estuary	1.0 km
	D	Depth of estuary	10 m
Earth	g	Acceleration due to gravity	9.81 m s^{-2}
	ω	M_2 angular frequency	1.4×10^{-4} s^{-1}
	f	Coriolis parameter	0 s^{-1}
Model	A_v	Vertical eddy viscosity parameter	1.0×10^{-3} m^2 s^{-1}
	s_f	Partial slip parameter	3.0×10^{-3} m s^{-1}
Forcing	A_{M_2}	M_2 amplitude at $x = 0$	1.0 m
	ϕ_{M_2}	M_2 phase at $x = 0$	0 deg

Table 3
The friction parameters used for the 2DH model in the narrow estuary example. For the traditional friction formulation, r_a is determined such that the best fit with the 3D model is achieved and for the 3D friction formulation, (r_a, φ_a) are computed directly from the 3D parameters given in Table 2.

	Traditional 2DH friction (Fitted)	3D friction (Calculated)
r_a	0.13	0.13
φ_a (deg)	0	28

Next, we compare the 2DH frictionless model with the 3D model. The phase of the frictionless model does not resemble the phase of the 3D model, but more strikingly, the amplitude is approximately 40 cm lower than in the frictional 3D model. Under the traditional 2DH friction formulation, increasing the friction always lowers the response of the estuary. However, under the 3D friction formulation, increasing the friction may lead to larger responses than the frictionless model. This implies that, there exist certain regions in the parameter space, where a 2DH model using the traditional friction formulation is never able to reproduce the water levels computed using a 3D model, irrespective of how one tries to calibrate the friction parameter. The mechanism responsible for this counter-intuitive result is explained using the amplification plane in Section 4.4.1. In the next section, the amplification plane is introduced.

4.4. Amplification plane

In the absence of the Coriolis force, the only difference between the 3D friction formulation and the traditional friction formulation is the phase shift φ_a. To study the effect of the phase shift φ_a on the water levels in the narrow barotropic estuary, the amplification plane is introduced. To this end, we consider the amplification a, which is defined as the ratio of the amplitude at the landward side and the forcing amplitude at the seaward side, see Supplementary Material S3 for details. For frictionally dominated systems, the amplification a tends

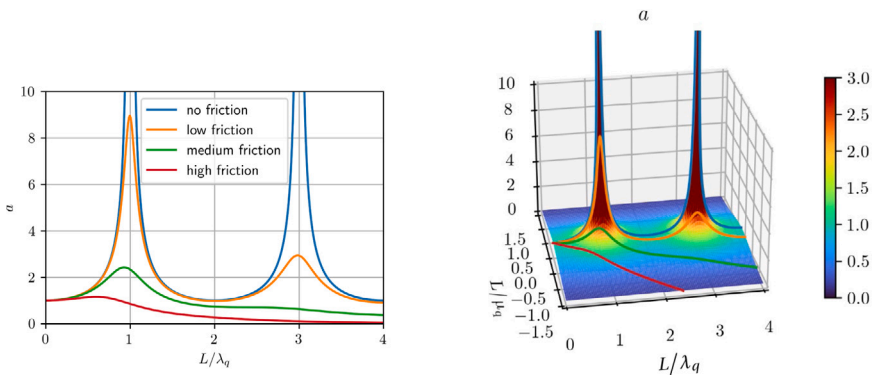

Fig. 5. Left, classical amplification curves as function of the nondimensional length of the estuary for no, low, medium and high friction values. These values are merely used to indicate the effect of increasing friction on the amplification. Right, the amplification plane as function of the nondimensional estuarine length with respect to the quarter wavelength and the quarter decay length scale. The classical amplification curves are also plotted in the amplification plane.

to zero, whereas for systems close to resonance, the amplification a tends to infinity.

As a first step, the amplification under the traditional friction formulation is considered. In the left panel of Fig. 5, classical amplification curves are shown as function of the nondimensional estuarine length L/λ_q, where L is the estuarine length and λ_q is the quarter wavelength of the frictionless tidal wave. For frictionless estuaries, pure resonance occurs when the estuarine length L is an odd multiple of the quarter tidal wavelength λ_q (see, e.g., Friedrichs, 2010; Roos et al., 2011). For frictional systems, the amplification close to the odd multiples attains a maximum and this maximum decreases as the nondimensional estuarine length increases.

The right panel of Fig. 5 shows the amplification plane where the x-axis represents the nondimensional estuarine length L/λ_q and the y-axis represents the nondimensional estuarine length L/μ_q, where μ_q is the quarter amplification length of the frictional tidal wave, which is defined as the length where the amplitude of the tidal free wave has increased by a factor $\exp(\pi/2) \approx 4.81$. Negative values indicate that the free tidal wave amplitude has decreased by the same factor. This x-y plane is related to the complex κL plane, where κ is the complex wavenumber, in particular, we have the relationship $\kappa L = \pi/2\,(L/\lambda_q + iL/\mu_q)$.

Given the model parameters, the pair (λ_q, μ_q) can be computed. Importantly, these parameters do not depend on the length of the estuary L. The position in the amplification plane can be determined by computing $(L/\lambda_q, L/\mu_q)$. Thus by varying the length of the estuary and keeping the other model parameters fixed, straight lines in the amplification plane are described. In the narrow rectangular estuary, the amplification a is fully determined by the nondimensional pair $(L/\lambda_q, L/\mu_q)$, see Supplementary Material S3 for details. Using this procedure, the no, low, medium and high friction curves are obtained that are shown on the right panel of Fig. 5.

4.4.1. The effect of the phase shift: in front of a resonance peak

In Section 4.3, we have shown an example where the water levels calculated with a 3D model cannot be replicated by a 2DH model using a traditional friction formulation. Here, we provide a general explanation of when this phenomenon may (or may not) occur, depending on the position in the amplification plane.

In this section, the model parameters are chosen such that the frictionless model is located in front of the first resonance peak, whereas in the next section, the parameters are chosen such that the frictionless model is located after the first resonance peak.

We consider three friction formulations: the frictionless formulation, the traditional 2DH friction formulation and the 3D friction formulation. Given the model parameters and friction formulation, the corresponding tidal wave length and decay length scale of the tidal wave can be computed (λ_q, μ_q). Using these two numbers, a location in the amplification plane can be identified that fully characterises the amplification within the estuary. This allows for the direct comparison of the effect of different friction formulations on the estuarine amplification.

To isolate the effect of the phase shift φ_a of the 3D friction formulation, it is assumed that φ_a is a free parameter that can be varied between $-180°$ and $180°$ without affecting the other parameters, whereas in reality φ_a is bounded between $0°$ and $45°$ and depends on the 3D parameters, see Supplementary Material S3.

In the left panel of Fig. 6, the first resonant peak in the amplification plane is shown together with the amplification computed using a frictionless, 2DH friction and 3D friction formulation, denoted by respectively the green, orange and blue dot. The purple curve is obtained by freely varying the phase shift parameter between $-180°$ and $180°$. By setting the phase shift to $\varphi_a = 0°$, the original 2DH formulation is recovered. For the 3D friction formulation the phase shift is chosen to be $45°$, the maximal allowable phase shift under the 3D friction formulation. Alternatively, when the 3D parameters are known, φ_a can be computed directly using Eq. (S1.14).

In the right panel of Fig. 6, the amplification along the purple curve in the amplification plane is shown as function of the phase shift parameter φ_a. The green line shows the amplification of the frictionless case, the orange dot signifies the amplification with the traditional 2DH friction formulation and the blue dot the amplification under the maximal allowable phase shift under the 3D friction formulation. Under the 3D friction formulation, the phase shift is between $0°$ and $45°$. If we increase the phase shift φ_a within this range the amplification increases. Even moderate values of the phase shift φ_a result in larger amplification than the frictionless case.

Thus, if the parameters of the frictionless model are chosen such that L/λ_q is smaller than and close enough to an odd number (i.e., in front of a resonance peak), then the model with 3D friction formulation with non-zero φ_a may be closer to resonance than the models without friction or with 2DH friction. To determine in which regions of the parameter space the phase shift and therefore 3D friction can be important, the right panel of Fig. 2 can be used (when neglecting the Coriolis force).

Now we are in a position to explain why the amplification under the 3D friction formulation can be larger than the amplification without friction, as observed in Section 4.3. We first compute the position of the frictionless model in the amplification plane $(L/\lambda_q, L/\mu_q) = (0.77, 0)$. Thus we are in front of the first resonance peak located at $(1, 0)$. Roughly speaking, adding 2DH friction (i.e, increasing r_a from 0 to 0.13, see Table 3) causes the position in the amplification plane to move towards the right (looking from the origin towards the first resonance peak). This is similar to the left panel of Fig. 6, starting from the green dot and moving towards the orange dot. The 3D friction formulation then tells us that we should approximately rotate this point $\varphi_a = 28°$ counter-clockwise (since the average amplitude r_a under the 3D friction

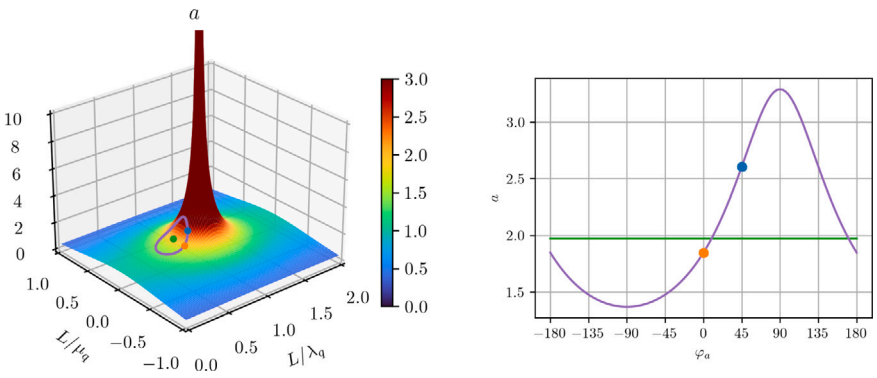

Fig. 6. Left, zoom in before the first resonance peak in the amplification plane with a frictionless, 2DH friction and 3D friction formulation denoted by the green, orange and blue dots. The purple curve shows the effect of varying φ_a assuming it is a free parameter. Right, the amplification is plotted as a function of the phase shift φ_a, assuming it is a free parameter. The green line represents the frictionless amplification. The orange and blue dot indicate the amplification using the 2DH traditional and 3D friction formulation, respectively.

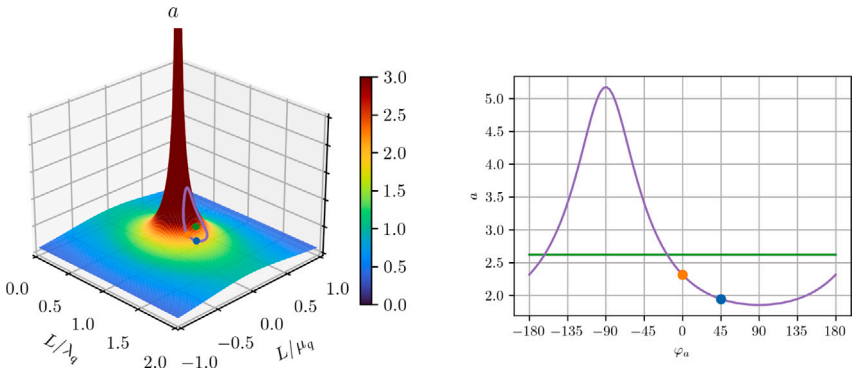

Fig. 7. Same as in Fig. 6 but the view has rotated 180 degrees such that we are looking just beyond the first resonance peak.

formulation remains the same, see Table 3). This causes the position in the amplification plane to move closer towards the first resonance peak. Hence, 3D friction can bring the system closer towards resonance than the frictionless model and, therefore, can exhibit larger amplification than the frictionless model. Referring to the left panel of Fig. 6, this is similar to moving from the orange dot along the purple line and stopping halfway between the orange and blue dot. In the right panel of Fig. 6, the same amplification curve is plotted as function of φ_a, allowing us to better compare the amplification under the different friction formulations.

4.4.2. *The effect of the phase shift: beyond a resonance peak*

In the left panel of Fig. 7, the amplification plane is shown just beyond the first resonance peak with again the green, orange and blue dot denoting the response under the frictionless, 2DH traditional and the 45° phase shifted 3D friction formulation. In this case we are looking from the first resonance peak towards to origin, i.e., the view has rotated by 180 degrees compared to Fig. 6. Increasing φ_a from the traditional 2DH friction formulation leads again to larger L/λ_q. However, in this case, increasing the phase shift φ_a leads to lower responses since increasing L/λ_q means moving away from the first resonance peak.

In the right panel of Fig. 7, the amplification as function of the phase shift φ_a is shown. This is the same amplification as experienced when traversing the purple curve in the left panel of Fig. 7. The frictionless response is shown by the green line, the orange dot indicates the traditional 2DH friction formulation response and the blue dot the amplification under a phase shift of 45°. This figure shows that increasing the phase shift φ_a leads to lower responses (within the physical range). This is in contrast to Section 4.3, where increasing the phase shift φ_a led to larger responses.

5. Discussion

Our results show that friction in a 3D model can lead to inherently different dynamics than friction in a 2DH model. In certain regions of the parameter space, 2DH models cannot even be calibrated to approximate the 3D results properly, as is illustrated in Section 4.3. This mismatch is primarily caused by the formation of a Stokes boundary layer near the bed. Such a layer is formed when both the Stokes number and the nondimensional parameter $\mathcal{A}$ are small.

The difference between linearised depth-averaged and depth-resolving models arises from the difference between the near-bed and depth-averaged velocity, leading to differing bed shear stresses and therefore dynamics. The literature mentions three aspects related to this discrepancy. 3D and 2DH friction may differ because the near-bed and depth-averaged velocity may differ in direction and magnitude due to 1) phase differences (Vreugdenhil, 1994), 2) Coriolis deflection (Mofjeld, 1980) and 3) frequency dependency (Zielke, 1966). We, for the first time, show how to consistently parametrise the effect of the depth in a 2DH model, including these three aspects, such that the same depth-averaged dynamics as in the depth-resolving model are described. This new parametrisation can be used in various geophysical systems where the effects of density are negligible such as well-mixed coastal seas and estuaries. Perhaps, this parametrisation can even be used in 2DH atmospheric models where the effects of Coriolis are often dominant.

This work focusses on the linear dynamics of the barotropic tide in shallow waters. The exact reduction from a linearised 3D model to a 2DH model is possible by exactly solving the 2DH closure problem: how to parametrise the near-bed velocity in terms of the depth-averaged velocity such that the depth-averaged dynamics are preserved? This exact reduction is possible under certain assumptions, which may not

always be satisfied. For example, the linearising the quadratic friction law and neglecting the advective terms is possible if the velocities are sufficiently small and the length scale sufficiently large. However, in various applications these conditions are not satisfied and care should be taken when these nonlinearities are important since the 3D friction formulation does not directly extend to these cases. Still, in the cases where we find that 2D and 3D friction are not too different, it is expected that this conclusion extends to a nonlinear model as well. In other cases, it is unclear if a parametrisation can be derived and this requires further research. Another simplifying assumption is the use of a vertically uniform eddy viscosity parameter. Ianniello (1977) has found that the solutions are not overly sensitive to the vertical eddy viscosity profile, except near the bed. This opens the door for further research to investigate how different near-bed eddy viscosity profiles affect the parametrisation of the near-bed velocity. It is expected that the methods and techniques described in this paper can still be used to analyse these cases.

6. Conclusion

In this paper, we have identified the differences in friction between a 3D and 2DH model and derived an exact friction formulation needed to reproduce the results of a linearised 3D model in a 2DH model. This required us to change the traditional friction parameter into a formulation that takes into account the past of the velocity signal. For harmonic signals, we have analysed in detail when these adaptations are important and this showed that it is especially important when the Stokes number is small. Furthermore, using the 3D friction formulation, a perfect match between the depth-averaged dynamics of two models is found, which was not possible under the traditional 2DH friction formulation. This indicates that the additional phase shift and cross-dependence of the friction terms can be important to correctly resolve the three-dimensional dynamics of the water motion.

CRediT authorship contribution statement

Marco P. Rozendaal: Writing – review & editing, Writing – original draft, Visualization, Validation, Methodology, Formal analysis, Conceptualization. **Yoeri M. Dijkstra:** Writing – review & editing, Supervision, Conceptualization. **Henk M. Schuttelaars:** Writing – review & editing, Supervision, Conceptualization.

Declaration of competing interest

The authors declare that they have no known competing financial interests or personal relationships that could have appeared to influence the work reported in this paper.

Data availability

No data was used for the research described in the article.

Acknowledgments

This work was supported by Flanders Hydraulics (WL2021 P20_007_1). The authors would like to thank the anonymous reviewers for their valuable comments and insights.

Appendix A. The bed shear stress relation

In this section, the bed shear stress relation based on the 3D model is derived. Winant (2007) and Kumar et al. (2016) have shown how to solve the vertical structure of the velocity profile analytically for a single tidal constituent with angular frequency ω. Since this parameter plays a crucial role in our derivation, we make this parametric dependence explicit using the notation ‘;ω’. Furthermore, we have found that a matrix notation is preferable for clarity and brevity. The matrix–vector form of the horizontal velocity vector with analytical vertical structure reads

$$\boldsymbol{U}(x,y,z;\omega) = \mathbf{P}\,\mathbf{c}(x,y,z;\omega)\,\mathbf{P}^{*}\,\nabla Z(x,y;\omega), \tag{A.1}$$

with the horizontal gradient operator given by $\nabla = (\partial_x, \partial_y)^T$, the constant unitary matrices read

$$\mathbf{P} = \frac{1}{\sqrt{2}}\begin{bmatrix} 1 & 1 \\ -i & i \end{bmatrix}, \quad \mathbf{P}^{*} = \frac{1}{\sqrt{2}}\begin{bmatrix} 1 & i \\ 1 & -i \end{bmatrix}, \tag{A.2}$$

and the vertical structure diagonal matrices for $\ell = 1, 2$ given by

$$c_{\ell\ell}(x,y,z;\omega) = \frac{g}{A_\nu \alpha_{\ell\ell}^2}\left\{ s_f \beta_{\ell\ell} \cosh\big(\alpha_{\ell\ell}(z-R)\big) - 1 \right\}, \tag{A.3}$$

with the diagonal matrices

$$\alpha_{\ell\ell}(x,y;\omega) = \sqrt{\frac{i\big(\omega + (-1)^{\ell+1} f\big)}{A_\nu}}, \tag{A.4}$$

$$\beta_{\ell\ell}(x,y;\omega) = \frac{1}{A_\nu \alpha_{\ell\ell} \sinh\big(\alpha_{\ell\ell} D\big) + s_f \cosh\big(\alpha_{\ell\ell} D\big)}. \tag{A.5}$$

Here, the subscript $\ell\ell$ denotes taking the ℓth diagonal element of the 2×2 matrices.

To derive an exact parametrisation for the bed shear stress, exact expressions for the near-bed and depth-averaged velocity are required. These can be obtained exactly since the vertical structure of the velocity profile is known analytically. The near-bed velocity is obtained by evaluating the vertical analytical velocity near the bed $z = -H$ and is given by

$$\boldsymbol{U}_b(x,y;\omega) = \mathbf{P}\,\mathbf{c}_b(x,y;\omega)\,\mathbf{P}^{*}\,\nabla Z(x,y;\omega), \tag{A.6}$$

with the vertical structure diagonal matrix evaluated near the bed $z = -H$ given by

$$c_{b,\ell\ell}(x,y;\omega) = \frac{g}{A_\nu \alpha_{\ell\ell}^2}\left\{ s_f \beta_{\ell\ell} \cosh\big(\alpha_{\ell\ell} D\big) - 1 \right\}. \tag{A.7}$$

The depth-averaged velocity is obtained by depth-averaging the vertical analytical velocity and reads

$$\overline{\boldsymbol{U}}(x,y;\omega) = \mathbf{P}\,\overline{\mathbf{c}}(x,y;\omega)\,\mathbf{P}^{*}\,\nabla Z(x,y;\omega), \tag{A.8}$$

with the depth-averaged diagonal matrix given by

$$\overline{c}_{\ell\ell}(x,y;\omega) = \frac{g}{A_\nu \alpha_{\ell\ell}^2}\left\{ \frac{s_f \beta_{\ell\ell}}{\alpha_{\ell\ell} D} \sinh\big(\alpha_{\ell\ell} D\big) - 1 \right\}. \tag{A.9}$$

The next step is using the exact expressions for the near-bed and depth-averaged velocity to obtain an exact parametrisation for the bed shear stress in the Fourier domain. We assume that there exists a complex-valued matrix $\mathbf{R}^{3D}$ such that we may express the bed shear stress in the Fourier domain in terms of the depth-averaged velocity as

$$s_f(x,y)\,\boldsymbol{U}_b(x,y;\omega) = \mathbf{R}^{3D}(x,y;\omega)\,\overline{\boldsymbol{U}}(x,y;\omega). \tag{A.10}$$

Substituting the exact expressions for the near-bed and depth-averaged velocities results in the following expression for the complex-valued friction matrix

$$\mathbf{R}^{3D}(x,y;\omega) = s_f(x,y)\,\mathbf{P}\,\boldsymbol{\Theta}(x,y;\omega)\,\mathbf{P}^{*}, \tag{A.11}$$

where we have defined the non-dimensional diagonal matrix

$$\boldsymbol{\Theta}_{\ell\ell}(x,y;\omega) = \frac{c_{b,\ell\ell}(x,y;\omega)}{\overline{c}_{\ell\ell}(x,y;\omega)}. \tag{A.12}$$

The entries of this non-dimensional matrix play a key role in the 3D friction formulation.

Using Eqs. (A.4), (A.5) and some algebra, it is found that the elements of this non-dimensional matrix may be expressed as

$$\Theta_{\ell\ell}(x,y;\omega) = \frac{-\mathcal{A}D_\ell^2}{1-\mathcal{A}D_\ell^2 - \dfrac{D_\ell}{\tanh D_\ell}}, \tag{A.13}$$

where we have identified two non-dimensional parameters

$$\mathcal{A}(x,y) = \frac{A_v}{s_f D}, \quad D_\ell(x,y;\omega) = \alpha_{\ell\ell} D. \tag{A.14}$$

The first non-dimensional parameter $\mathcal{A}$ is the ratio between the vertical eddy viscosity A_v and the product of the partial-slip parameter s_f and the depth D. This non-dimensional parameter may be derived from the partial-slip boundary condition. The second non-dimensional parameter is the product of the vertical decay length scale $\alpha_{\ell\ell}$ and the depth D. This non-dimensional parameter is complex-valued and its modules is inversely proportional to the Stokes number. Importantly, the second non-dimensional number depends on the frequency ω due to the frequency dependence of $\alpha_{\ell\ell}$.

For the computations, the complex nondimensional number D_ℓ is used. However, for interpretation purposes we may write this complex number in polar form using two real-valued nondimensional parameters

$$D_{1,2} = \frac{1}{\mathrm{Stk}_\pm}\exp\left(i\pi/4\,\mathcal{P}_\pm\right), \tag{A.15}$$

with the real-valued nondimensional parameters given by

$$\mathrm{Stk}_\pm(x,y;\omega) = \frac{1}{D}\sqrt{\frac{A_v}{|\omega \pm f|}}, \quad \mathcal{P}_\pm = \mathrm{sign}(\omega \pm f). \tag{A.16}$$

The index $\ell = 1$ corresponds to the + sign and the index $\ell = 2$ corresponds to the − sign.

The elements of the 3D friction matrix are found by expanding the matrices in Eq. (A.11) and this yields

$$\mathbf{R}^{3D}(x,y;\omega) = s_f\,\frac{1}{2}\begin{bmatrix} \Theta_{11}+\Theta_{22} & i(\Theta_{11}-\Theta_{22}) \\ -i(\Theta_{11}-\Theta_{22}) & \Theta_{11}+\Theta_{22} \end{bmatrix}. \tag{A.17}$$

The elements of this matrix can be expressed in polar form as

$$\mathbf{R}^{3D}(x,y;\omega) = s_f\begin{bmatrix} r_1 e^{i\varphi_1} & -r_2 e^{i\varphi_2} \\ r_2 e^{i\varphi_2} & r_1 e^{i\varphi_1} \end{bmatrix}, \tag{A.18}$$

where we have defined the amplitudes and phases

$$r_1 = \frac{1}{2}\left|\Theta_{11}+\Theta_{22}\right|, \qquad r_2 = \frac{1}{2}\left|\Theta_{11}-\Theta_{22}\right|, \tag{A.19}$$

$$\varphi_1 = \arg(\Theta_{11}+\Theta_{22}), \qquad \varphi_2 = -\frac{\pi}{2} + \arg(\Theta_{11}-\Theta_{22}). \tag{A.20}$$

No coriolis

The 3D friction matrix simplifies if there is no Coriolis force ($f = 0$). In this case, the coefficient $\alpha_{\ell\ell}$ becomes independent of the index ℓ, thus $\alpha_{11} = \alpha_{22}$. Since all the other coefficients only depend on the index ℓ through the $\alpha_{\ell\ell}$'s, it follows that all coefficients become ℓ independent. As a consequence, we have $\Theta_{11} = \Theta_{22}$ and, therefore,

$$\mathbf{R}^{3D}(x,y;\omega) = s_f\begin{bmatrix} \Theta_{11} & 0 \\ 0 & \Theta_{11} \end{bmatrix} = s_f\Theta_{11}\mathbf{I}_2. \tag{A.21}$$

The polar form of the elements simplifies to

$$r_1 = |\Theta_{11}|, \quad r_2 = 0, \quad \varphi_1 = \arg(\Theta_{11}), \quad \varphi_2 = -\frac{\pi}{2}. \tag{A.22}$$

The relevant parameters in this case are r_1 and φ_1. The parameter φ_2 is not relevant in the no Coriolis case since $r_2 = 0$.

Appendix B. Supplementary data

Supplementary material related to this article can be found online at https://doi.org/10.1016/j.ocemod.2024.102330.

References

Batchelor, G.K., 1967. An Introduction to Fluid Dynamics. Cambridge University Press, Cambridge.

Chekhova, M., Banzer, P., 2021. Polarization of Light in Classical, Quantum, and Nonlinear Optics. De Gruyter.

Cushman-Roisin, B., Beckers, J.-M., 2009. Introduction to Geophysical Fluid Dynamics: Physical and Numerical Aspects. Academic Press.

Defant, A., 1961. Physical Oceanography. Pergamon, New York.

Dijkstra, Y., 2019. Regime Shifts in Sediment Concentrations in Tide-Dominated Estuaries (Ph.D. thesis). Delft University of Technology, http://dx.doi.org/10.4233/uuid:28e12122-9c63-4260-aa87-b9e8f7de35fe.

Dingemans, M., 1997. Water Wave Propagation over Uneven Bottoms: Linear Wave Propagation. World Scientific Publishing.

Dyer, K.R., 1974. The salt balance in stratified estuaries. Estuar. Coast. Mar. Sci. 2 (3), 273–281. http://dx.doi.org/10.1016/0302-3524(74)90017-6.

Fischer, H.B., 1972. Mass transport mechanisms in partially stratified estuaries. J. Fluid Mech. 53 (4), 671–687. http://dx.doi.org/10.1017/S0022112072000412.

Friedrichs, C.T., 2010. Barotropic tides in channelized estuaries. In: Valle-Levinson, A. (Ed.), Contemporary Issues in Estuarine Physics. Cambridge University Press, Cambridge, pp. 27–61. http://dx.doi.org/10.1017/CBO9780511676567.

Garrett, C., 1975. Tides in gulfs. Deep-Sea Res. Oceanogr. Abstracts 22 (1), 23–35. http://dx.doi.org/10.1016/0011-7471(75)90015-7.

Glock, K., Tritthart, M., Habersack, H., Hauer, C., 2019. Comparison of hydrodynamics simulated by 1D, 2D and 3D models focusing on bed shear stresses. Water 11 (2), 30–37. http://dx.doi.org/10.3390/w11020226.

Hulscher, S.J., 1996. Tidal-induced large-scale regular bed form patterns in a three-dimensional shallow water model. J. Geophys. Res.: Oceans 101 (C9), 20727–20744. http://dx.doi.org/10.1029/96JC01662.

Huthnance, J.M., 1980. On shelf-sea 'resonance' with application to Brazilian M3 tides. Deep Sea Res. A, Oceanogr. Res. Pap. 27 (5), 347–366. http://dx.doi.org/10.1016/0198-0149(80)90031-X.

Ianniello, J.P., 1977. Tidally induced residual currents in estuaries of constant breadth and depth. J. Phys. Oceanogr. 35 (4), 755–786.

Kumar, M., Schuttelaars, H.M., Roos, P.C., Möller, M., 2016. Three-dimensional semi-idealized model for tidal motion in tidal estuaries: An application to the Ems estuary. Ocean Dyn. 66 (1), 99–118. http://dx.doi.org/10.1007/s10236-015-0903-1.

Li, C., O'Donnell, J., 1997. Tidally driven residual circulation in shallow estuaries with lateral depth variation. J. Geophys. Res. C: Oceans 102 (C13), 27915–27929. http://dx.doi.org/10.1029/97JC02330.

Marinone, S.G., 2000. Tidal currents in the Gulf of California: Intercomparisons among two- and three-dimensional models with observations. Ciencias Mar. 26 (2), 275–301. http://dx.doi.org/10.7773/cm.v26i2.579.

Mofjeld, H.O., 1980. Effects of vertical viscosity on kelvin waves. J. Phys. Oceanogr. 10 (7), 1039–1050. http://dx.doi.org/10.1175/1520-0485(1980)010<1039:eovvok>2.0.co;2.

Pope, S.B., 2000. Turbulent Flows. Cambridge University Press, Cambridge, http://dx.doi.org/10.1017/CBO9780511840531.

Prandle, D., 1982. The vertical structure of tidal currents. Geophys. Astrophys. Fluid Dyn. 22 (1–2), 29–49. http://dx.doi.org/10.1080/03091928208221735.

Roos, P.C., Velema, J.J., Hulscher, S.J., Stolk, A., 2011. An idealized model of tidal dynamics in the North Sea: Resonance properties and response to large-scale changes. Ocean Dyn. 61 (12), 2019–2035. http://dx.doi.org/10.1007/s10236-011-0456-x.

Schramkowski, G.P., De Swart, H.E., 2002. Morphodynamic equilibrium in straight tidal channels: Combined effects of Coriolis force and external overtides. J. Geophys. Res.: Oceans 107 (12), http://dx.doi.org/10.1029/2000jc000693.

Schramkowski, G.P., Schuttelaars, H.M., Swart, H.E.D., 2002. The effect of geometry and bottom friction on local bed forms in a tidal embayment. Cont. Shelf Res. 22, 1821–1833.

Soulsby, R.L., 1981. Measurements of the Reynolds stress components close to a marine sand bank. Mar. Geol. 42 (1–4), 35–47. http://dx.doi.org/10.1016/0025-3227(81)90157-2.

Soulsby, R.L., 1983. The bottom boundary layer of shelf seas. In: Johns, B. (Ed.), Physical Oceanography of Coastal and Shelf Seas. Elsevier, Amsterdam.

Souza, A.J., 2013. On the use of the Stokes number to explain frictional tidal dynamics and water column structure in shelf seas. Ocean Sci. 9 (2), 391–398. http://dx.doi.org/10.5194/os-9-391-2013.

Souza, A.J., Simpson, J.H., 1996. The modification of tidal ellipses by stratification in the Rhine ROFI. Cont. Shelf Res. 16 (8), 997–1007. http://dx.doi.org/10.1016/0278-4343(95)00042-9.

Stacey, M.T., Burau, J.R., Monismith, S.G., 2001. Creation of residual flows in a partially stratified estuary. J. Geophys. Res.: Oceans 106 (C8), 17013–17037. http://dx.doi.org/10.1029/2000JC000576.

Taylor, G.I., 1921. Tidal oscillations in gulfs and rectangular basins. Proc. Lond. Math. Soc. 20 (1), 148–181.

Van Rijn, L.C., 2010. Tidal Phenomena in the Scheldt Estuary. Technical Report, Deltares, pp. 1–99, URL: http://www.vliz.be/imisdocs/publications/214759.pdf.

Vreugdenhil, C.B., 1994. Numerical Methods for Shallow-Water Flow. Kluwer Academic Publishers, Dordrecht, http://dx.doi.org/10.1007/978-94-015-8354-1.

Winant, C.D., 2007. Three-dimensional tidal flow in an elongated, rotating basin. J. Phys. Oceanogr. 37 (9), 2345–2362. http://dx.doi.org/10.1175/JPO3122.1.

Wong, K.-C., 1994. On the nature of transverse variability in a coastal plain estuary. J. Geophys. Res. 99 (C7), 14209. http://dx.doi.org/10.1029/94JC00861.

Zielke, W., 1966. Frequency Dependent Friction in Transient Pipe Flow (Ph.D. thesis). University of Michigan.